King's Research Portal

[Link to publication record in King's Research Portal](#)

The mechanical stability of proteins regulates their translocation rate into the cell nucleus

Elvira Infante[1†], Andrew Stannard[1†], Stephanie J. Board[1], Palma Rico-Lastres[1], Elena Rostkova[1], Amy E.M. Beedle[1], Ainhoa Lezamiz[1], Yong Jian Wang[1], Samuel Gulaidi Breen[1], Fani Panagaki[1], Vinoth Sundar Rajan[1], Catherine Shanahan[2], Pere Roca-Cusachs[3] and Sergi Garcia-Manyes[1,4]*

[1]Department of Physics, Randall Centre for Cell and Molecular Biophysics, and London Centre for Nanotechnology, King's College London, WC2R 2LS, London, UK.
[2]Cardiovascular Division, James Black Centre, King's College London, London SE5 9NU, UK
[3]Institute for Bioengineering of Catalonia (IBEC), The Barcelona Institute of Science and Technology (BIST), and University of Barcelona, 08028 Barcelona, Spain
[4]The Francis Crick Institute, 1 Midland Road, London, NW1 1AT, UK

[†]These authors contributed equally to the work
*Correspondence: S.G.-M. (sergi.garcia-manyes@kcl.ac.uk)

Abstract

The translocation of mechanosensitive transcription factors across the nuclear envelope is a crucial step in cellular mechanotransduction. Yet the molecular mechanisms by which mechanical cues control the nuclear shuttling dynamics of transcription factors through the nuclear pore complex to activate gene expression are poorly understood. Here, we show that the nuclear import rate of myocardin-related transcription factor A (MRTFA) — a protein that regulates cytoskeletal dynamics via the activation of the serum response factor— inversely correlates with the protein's nanomechanical stability and does not relate to its thermodynamic stability. Tagging MRTFA with mechanically-stable proteins results in the downregulation of gene expression and subsequent slowing down of cell migration. We conclude that the mechanical unfolding of proteins regulates their nuclear translocation rate, and highlight the role of the nuclear pore complex as a selective mechanosensor able to discriminate forces as low as ~10 pN. The modulation of the mechanical stability of transcription factors may represent a new, general strategy for the control of gene expression.

Cellular mechanotransduction requires that cytoplasmic mechanical cues are relayed to the nucleus to activate gene expression[1]. Several transcription factors, such as YAP/TAZ[2], β-catenin[3] or zyxin[4], have emerged as important mediators of mechanical signalling[5]. The myocardin related transcription factor A (MAL/MRTFA) stimulates the transcriptional activity of the serum response factor (SRF)[6], which targets genes that encode cytoskeletal components[7,8], including actin and other key proteins involved in cell motility, adhesion and differentiation[9]. Importantly, the Rho-dependent MRTFA/SRF activity is shown to control migration and invasion of metastatic cancer cell lines[6]. Thorough *in-vitro* cell-biology assays, supported by structural-biology approaches, have provided a seemingly complete picture of how MRTFA localization is regulated at the biochemical level[10]; in serum-starved cells, MRTFA is mostly cytoplasmic and bound to G-actin. Upon serum stimulation, Rho-GTPases trigger F-actin polymerization[11] and the subsequent dissociation of G-actin from the MRTFA RPEL motif results in the exposure of a nuclear localization sequence (NLS)[12] that signals MRTFA to translocate into the nucleus[13]. Consequently, the active remodelling of the cytoskeleton is tightly controlled by a Rho/actin-mediated mechanical feedback mechanism upstream of MRTFA/SRF transcriptional activity. Given that mechanical cues control both its cytoplasmic[10] and nuclear[14,15] activity, MRTFA is an excellent molecular platform to interrogate whether nuclear shuttling of transcription factors through the nuclear pore complex (NPC) — the primary transport gate for molecular exchange to and from the nucleus[16] — is also *per se* a mechanically-activated process, with potential knock-on effects at the transcriptional and functional levels.

Recent single-molecule nanomechanical experiments on molecular pores showed that the translocation of polypeptides through the ClpX proteolytic *E. coli* machinery requires mechanical unfolding[17], and that the pulling direction and mechanical stability of the degraded protein[18] regulate its translocation kinetics. Similarly, proteins need to unfold before they cross nanopores upon electrical stimulation[19]. Unlike the narrow pores of the ClpX and α-hemolysin proteins, recent cryo-EM structures revealed that the central pore of the human NPC, such as that of U2OS cells[20], is rather large (~40-50 nm width)[21] in comparison to the size of the translocating cargo. Despite its considerable size and the absence of known direct ATP consumption, transport across the NPC is extremely selective and finely regulated by a sophisticated set of intrinsically disordered[22] and highly dynamic nucleoporins (Nups), rich in phenylalanine-glycine (FG) motifs, that line the central NPC channel and extend filaments on both the cytoplasmic and nucleoplasmic faces[23]. These FG-Nups form a dense protein mesh that acts as an effective 'molecular sieve'[24]. Several complementary models — including the virtual gating[25], polymer brush[26], selective gel phase[27], forest[30], bimodal structure[28], and reduction of dimensionality[29] models— have been proposed to explain the physical basis for the high selectivity and directionality observed during transport across the NPC, on the basis of the physicochemical properties of nucleoporins[23,24]. The general consensus is that translocating molecules need to overcome an entropic energy barrier created by the rapidly-fluctuating FG-Nups[30]. Given that mechanical unfolding and extension drastically reduces the entropy of proteins[31], it is tempting to speculate that a mechanically-extended protein cargo will traverse the repulsive mechanical gate more efficiently than the protein's natively-folded stiffer conformation, exhibiting a much higher degree of steric hindrance. Early independent

observations reported that ribonucleoprotein particles are straightened while translocating through the NPC[32], and that the transport of flexible cargos is faster than rigid ones of similar size[23,33-35]. More recently, we demonstrated that the nuclear translocation of the YAP transcription factor is mechanoselective[36]. Motivated by these findings, we conjectured that the mechanical unfolding of proteins could enhance their dynamics of nuclear import, having potential knock-on effects at the genetic and functional levels. Here we employed a multiscale experimental approach, using a combination of single-molecule force spectroscopy, live-cell imaging, optogenetics, gene expression, and cellular-motility assays to quantitatively investigate the mechanosensor role of the NPC in regulating the dynamics of MRTFA translocation.

Serum stimulation triggers nuclear accumulation of MRTFA[10]. To examine the dynamics of MRTFA nuclear translocation of serum-starved U2OS cells after 15% serum stimulation (Figs. 1A & S1) we used live-imaging confocal microscopy to monitor the fraction of nuclear MRTFA-GFP for 20 minutes following stimulation (Fig. 1B). Fitting the resulting time course with a single exponential yielded a rate constant $k = 3.91\pm0.42 \times 10^{-3}\,s^{-1}$ and equilibrium nuclear accumulation $n_e = 78.4\pm1.9$ % (Fig. S2). Since MRTFA is known to be in dynamic equilibrium between the cytoplasm and the nucleus[10], we decoupled the contributions of the import and export processes, both being treated as pseudo-first order processes (see SI), to yield import and export rate constants of $k_I = 3.07\pm0.32 \times 10^{-3}\,s^{-1}$ and $k_E = 0.84\pm0.14 \times 10^{-3}\,s^{-1}$ respectively. This dynamic equilibrium was demonstrated by treating starved cells with leptomycin B, known to block nuclear export[37], resulting in gradual nuclear accumulation of MRTFA-GFP (Fig. S3).

To explore the effect of the mechanical stability of the translocating protein on its shuttling dynamics, the most common tactic would entail the rational modification of its mechanical stability via the introduction of well-defined point mutations into the force-bearing structural motif[38]. Unfortunately, the structural information of MRTFA is limited to its relatively small RPEL motif[13]. We hence used an alternative strategy that consisted of concatenating fluorescent MRTFA constructs with different protein domains with varying mechanical stabilities. As a first candidate we chose the major pilin of *S. pyogenes*, the two-domain protein Spy0128. Each domain of Spy0128 contains an intermolecular isopeptide bond (Lys^{36}–Asn^{168} and Lys^{179}–Asn^{303} in the N- and C- domains respectively), with each bond linking residues close to either termini of each domain[39] (Fig. 1C), preventing mechanical extensibility. Indeed, single molecule force spectroscopy experiments have demonstrated that Spy0128 is one of the most mechanically-stable protein known[40]. The formation of these isopeptide bonds, which lock the protein in its native conformation, are catalysed by nearby glutamic acid residues, specifically E117A and E258A in the N- and C- domains, respectively[41]. Point mutations of these residues abrogate isopeptide bond formation, and the resulting protein mutants become suddenly extensible upon mechanical unfolding[40]. We compared the nuclear translocation kinetics of MRTFA-Spy0128$_{WT}$-GFP with the corresponding E117A and E258A mutants (Figs. 1D & S4). U2OS cells expressing MRTFA tagged with the mechanically-inextensible Spy0128$_{WT}$ exhibited slow nuclear import and limited nuclear accumulation. By contrast, both the E117A and E258A mutants led to dramatically faster import without influence on the export rate (Fig. 1E), resulting in greater nuclear accumulation. These results suggest that the rate of nuclear translocation

correlates with the ability of the tagging protein to unfold. However, given that this pilin system is an extreme case where the isopeptide bond acts as a 'binary' unfolding switch, we speculated that the dynamics of nuclear shuttling could follow a continuous trend with the mechanical stability of the translocating protein.

To test this hypothesis, we used 3 distinct immunoglobulin (Ig) domains – namely Ig1, Ig27 and Ig32 – from cardiac titin (Fig. 2A). This giant protein is responsible for the passive elasticity of muscle and its mechanical stability – increasing along the N-C termini direction[42] – can be directly characterized in single molecule force spectroscopy (SMFS) experiments. To this goal, polyproteins of the different Ig domains under study, namely (Ig1-Ig27$_{C47A-C63A}$)$_4$, (Ig27$_{WT}$)$_8$ and (Ig32)$_8$, were individually stretched by an AFM cantilever at a constant velocity of 400 nm s^{-1} (Fig. 2B), resulting in the classic saw-tooth pattern of mechanical unfolding, whereby each force peak fingerprints the unfolding of an individual domain within the polyprotein chain (Fig. 2C). As expected, the mechanical stability of the Ig1 domain, located in the proximal region of titin's elastic I-band, displays a lower mechanical stability (144±27 pN) than the Ig27 (207±29 pN) and Ig32 (267±33 pN) domains, which are situated further down in the distal I-band (Figs. 2D & S5). These results are all in general agreement with previous findings[42-44].

Having characterized the mechanical stability of each Ig domain independently, we measured the nuclear translocation kinetics of each MRTFA-X-BFP construct, with X = Ig1 (Fig. 1G), Ig27 or Ig32. Tagging MRTFA with the mechanically-labile Ig1 resulted in much faster translocation (and much higher nuclear accumulation) than Ig27 and Ig32 (Figs. 2E & S6). The nuclear import rate constant exhibits behaviour in line with an exponential dependence with the unfolding force measured by SMFS (Fig. 2F). By contrast, the export rate constant is largely independent of the mechanical stability of the tagging domain. We then investigated the translocation kinetics of MRTFA tagged with a domain of extremely low mechanical stability (albeit with a different fold and molecular weight) – the mechanically-labile R16 domain of spectrin[45] (Fig. S7). MRTFA-R16-GFP exhibits the largest import rate constant (k_I = 4.26±0.45 ×10^{-3} s^{-1}) of any of the probed chimeric MRTFA constructs. Taken together, these experiments suggest that the dynamics of MRTFA nuclear accumulation inversely correlate with the mechanical-stability hierarchy of the tagging domains.

Although the different titin Ig domains share a similar Ig fold and are of comparable size, their sequences are different, and the differences in mechanical stability are rather large (~60 pN, Fig. 2D). An ideal comparison of the effect that a change in the protein's mechanical stability has on the rate of nuclear translocation should be done, *stricto sensu*, by modulating the protein's mechanical stability while keeping its sequence, size, and structure largely unperturbed. With this purpose, we repeated the live-cell imaging experiments using MRTFA-Ig27$_X$-GFP constructs, with the Ig27$_X$ domain either wild-type (X = WT) or harbouring a point mutation in a well-localized position within the mechanical clamp, namely X = V13P, V11P, V15P, or Y9P – all inducing a change in the mechanical stability, in the order V13P < V11P < V15P < WT < Y9P[38] (Fig. 3A). The dynamics of nuclear accumulation for each construct also followed the mechanical stability trend (Figs. 3B & 3C) and, strikingly, the import rate constant is again found to display an exponential

dependence on the unfolding force from constant velocity SMFS measurements[38] (Fig. 3D), whereas the export rate does not display any dependence on unfolding force (Fig. S8).

We next independently confirmed the nuclear import dependence (and the nuclear export independence) on mechanical stability observed in our translocation kinetic analysis. First, we compared the nuclear accumulation (solely dictated by the import process) of MRTFA-Ig27$_{WT}$-GFP and MRTFA-Ig27$_{V13P}$-GFP in serum-starved U2OS cells in the presence of leptomycin B, which blocks nuclear export. As expected, the mechanically-labile V13P construct exhibits faster nuclear accumulation than the mechanically-stable WT form (Figs. 3E & S9) –corroborating the inverse correlation between nuclear import and mechanical stability. Using the same MRTFA constructs, we then conducted fluorescence loss in photobleaching (FLIP) experiments[11] on serum-stimulated U2OS cells to measure the decay in nuclear fluorescence intensity following photobleaching of a localised cytoplasmic region (Figs. 3F & S10). The nuclear intensity decay at early times (when export dominates) for both constructs overlaps within error, further demonstrating that nuclear export is insensitive to the mechanical properties of the translocating protein.

To learn whether the nuclear import rate also correlated with the thermodynamic stability of each tagging domain, we conducted differential scanning fluorimetry of all Ig27 variants and found no correlation between their melting temperature and mechanical stability (Figs. 3D & S11) – notably, the Y9P mutant has an increased mechanical stability, and yet exhibits a marked decrease in the thermal stability, with respect to the wild-type. These experiments unambiguously demonstrated that nuclear import is dictated by the mechanical – and not the thermal – stability of the translocating protein. Analogous experiments comparing the nuclear translocation for MRTFA-Ig27$_{WT}$-GFP and MRTFA-Ig27$_{V13P}$-GFP in MDA-MB-231 and HeLa cells (Fig. S12 and S13) led to similar conclusions, indicating the mechanical selectivity of the import mechanism might be general and independent of cell line.

To directly demonstrate the differential sensitivity to protein nanomechanics within a single cell, we conducted control experiments whereby U2OS cells were co-transfected with MRTFA-Ig27$_X$-BFP and MRTFA-Ig27$_Y$-YFP constructs, where X, Y = V11P, V13P, V15P, WT, or Y9P. The choice of BFP and YFP ensured that both emission wavelengths were sufficiently far apart to guarantee their individual detection without cross-talk, while presumably exhibiting very close (if not identical) mechanical stabilities[46]. This is confirmed as the translocation behaviour of MRTFA constructs differing only in their fluorescent tag display near identical behaviour (Fig. S14). Dual fluorescence live-cell imaging to simultaneously monitor the nuclear translocation of MRTFA-Ig27$_{WT}$-BFP and MRTFA-Ig27$_{V11P}$-YFP (Fig. 3G) showed that the nuclear import rate of the mechanically-labile V11P construct was significantly higher than that of the mechanically-stable WT construct (Fig. 3H and inset), with no significant difference in the export rate. As expected, transport was completely blocked by overexpression of the dominant-negative vector of RanGTP, RanQ69L-mCherry (Fig. S15). Importantly, treatment with importazole, a small molecule inhibitor of importin-β[47], noticeably inhibits overall translocation, without affecting selectivity (Fig. S15). Finally, the kinetic analysis of multiple dual fluorescence assays comparing MRTFA-Ig27$_X$-BFP constructs benchmarked against MRTFA-Ig27$_{V13P}$-YFP (or MRTFA-Ig27$_{V11P}$-YFP) confirmed the mechanical hierarchy observed for the different Ig27

mutants when analysed independently (Figs. 3I & S14). In conclusion, these experiments reiterate the high degree of mechanical sensitivity underpinning the nuclear translocation of MRTFA.

To examine whether the mechanical sensitivity to nuclear import is independent of MRTFA, we conducted optogenetic experiments using U2OS cells transiently expressing protein constructs containing the light-inducible nuclear export probe, LEXY (*As*LOV2-NES)[48]. Specifically, we monitored the translocation of NLS-Ig27$_X$-mCherry-LEXY where X = WT or V13P (Figs. 4 & S16). In the absence of light (dark state), the NES of LEXY is docked with the LOV domain, preventing exportin binding and, therefore, active nuclear export. Upon illumination with blue light, the LOV domain undergoes a conformational change that exposes the NES motif, resulting in the fast exclusion of the construct from the nucleus. The reversibility of the process is confirmed when the blue light is subsequently switched off, and nuclear localisation is recovered. Comparing the dark-state nuclear translocation kinetics of the optogenetic constructs tagged with Ig27 variants (Figs. 4C & S16) revealed that the nuclear import rate of the mechanically-labile V13P construct ($k_I = 1.20\pm0.08 \times10^{-3}$ s^{-1}) was significantly higher than the mechanically-stable WT construct ($k_I = 0.900\pm0.063 \times10^{-3}$ s^{-1}) (Fig. 4D). By contrast, the nuclear export rate did not significantly vary between these constructs. These experiments, demonstrating the high mechanical selectivity of nuclear import of proteins across the NPC, underscored the generality of our findings.

Given that MRTFA regulates serum response factor (SRF)-related genes[6], we posed the question of whether variations in the mechanical stability of the translocating MRTFA constructs had a direct impact on gene expression. Previous work reported that the myosin light chain 9 gene (MYL9), actin (ACTB), and SRF itself, responsible for cell migration and cancer invasion, are all regulated by MRTFA/SRF[6,49]. We conducted quantitative polymerase chain reaction (qPCR) experiments on stable U2OS cell lines expressing MRTFA-GFP and measured, 4 hours after serum stimulation, an increase in the expression of MYL9, ACTB, and SRF compared to cells stably expressing a GFP-empty vector (Fig. 5A). Most importantly, cells stably expressing MRTFA-Ig27$_{V13P}$-GFP exhibited higher levels of MYL9, ACTB, and SRF mRNA expression compared to an MRTFA-Ig27$_{WT}$-GFP stable cell line (Fig. 5A). Importantly, all our stable cell lines express similar levels of exogenous MRTFA (and a 2-fold increase with respect to the endogenous MRTFA, Fig. S13). Triggered by these observations, we then hypothesized that the variations in gene expression could potentially translate into functional consequences at the cellular level. Since MRTFA upregulates a variety of genes involved in cell migration, we postulated that the cells expressing MRTFA constructs tagged with a mechanical-labile domain – resulting in enhanced nuclear accumulation – would migrate faster than cells where MRTFA was tagged with a mechanically-stable domain. To test this premise, we conducted wound-healing assays on the U2OS stable cell lines described above. These experiments showed that the 24-hour wound recovery of cells expressing the mechanically-labile MRTFA-Ig27$_{V13P}$-GFP construct was significantly higher than that of cells expressing the mechanically-stable MRTFA-Ig27$_{WT}$-GFP construct (Figs. 5B, 5C, & S17). Finally, we conducted cell motility assays on MDA-MB-231 cells[6], and tracked, for 13 hours, the migration speed of individual cells transfected with different MRTFA constructs (Fig. S17). Notably, the levels of MRTFA overexpression is the same throughout the different constructs, and similar to the endogenous levels (Fig. S13). In this case we also

7

observed that cells transfected with the MRTFA construct harbouring the $Ig27_{V13P}$ domain moved significantly faster than those containing $Ig27_{WT}$ (Fig. 5D). Combined, these assays demonstrate that very subtle changes in the mechanical stability of translocating proteins has large effects at gene expression level (Fig. 5E), ultimately controlling the motility of two cancer cell lines.

While recent structural advances have provided invaluable information on the composition and spatial arrangement of the multifaceted NPC machinery[16,50,51], dynamic measurements of the NPC have proved challenging, especially due to the intrinsically-disordered and highly-mobile nature of the unstructured FG-Nup domains. Pioneering studies using AFM imaging measured the nanoscopic spatiotemporal dynamics of FG-Nups[26], and probed the nanomechanical repulsion of the NPC central channel[52]. However, direct measurement of molecular transport at the nanoscale has lagged significantly behind. Our multiscale experiments revealed that transport across the NPC inversely correlates with the mechanical stability of the shuttling protein.

This scenario is compatible with the current models of nucleocytoplasmic transport, both from a physical and chemical perspective. From a polymer physics view, mechanically-unfolded conformations might be able to surf the intricate and dense NPC FG-Nup 'forest' more efficiently than the sterically-bulkier folded counterpart. This picture would be compatible for example with the selective phase model[24], whereby the 'adaptive' barrier would not need to dramatically open to let the 'floppier' mechanically-unfolded protein through. Similarly, within the FG-gel context[24], it is easy to rationalise that unfolded proteins are likely to be more efficient at crossing smaller mesh sizes, thereby minimising transient kinetic traps. Considering the interactions established during nuclear shuttling, a very recent elegant report demonstrated that the nature of the surface chemical properties of proteins determines their passage rates across the NPC[53]; while negatively-charged residues and lysines hinder passage, hydrophobic residues, certain polar residues and arginines dramatically increase the passage efficiency as a result of the favourable interactions established with the FG-Nups. Although this rationale explains the high hydrophobic content of the nuclear transport receptors, it also applies to the nature of the translocating protein cargos[53]. In particular, folded globular proteins tend to bury their hydrophobic residues in the solvent-inaccessible core. Hence, we postulate that upon mechanical unfolding, the otherwise cryptic hydrophobic residues will be readily exposed, facilitating their interaction with the dynamic FG-Nups and resulting in an overall increase of their translocation rate. Of note, while our experiments show that those proteins with lower mechanical stability translocate faster, it is likely, as observed in the slow nuclear translocation of the inextensible $Spy0128_{WT}$ construct, that, while speeding up the process, mechanical unfolding is not mandatory[23] to cross the NPC. Lacking a described ATP-dependent machinery, it remains unresolved what is effectively pulling on the translocating proteins. While the highly-dynamic Nups seem the first candidates to attach and pull from one of the protein's termini, given the large (~30) number of different FG-Nups, it is difficult to anticipate the precise FG-Nup(s) responsible for the mechanical interaction. An educated structurally-based guess would suggest that those Nups forming the cytoplasmic ring, such as the Nup214–Nup88–Nup62 complex, or even the central Nup358, might play a crucial

role[51]. Future work based on characterising the effect of the major Nup families on nuclear mechanotranslocation will help shed direct light into this question.

A central discovery in our experiments is that the import rate constant of the different constructs (Figs. 2G & 3D) displays an exponential dependency with the unfolding force measured via SMFS when proteins are stretched at 400 nm s^{-1}. Despite the clear mechanical trend that we measured, this does not entail that the absolute magnitude of the forces experienced in our cell experiments are the same as those measured in the *in vitro* single molecule AFM experiments, performed under non-equilibrium conditions at high pulling velocities in a buffer and experimental setting that differ from the physiological native environment of the NPC, where the forces experienced are likely to be much lower and applied over much longer time periods. Strikingly, the hierarchy in the mechanical stability measured in the AFM experiments is maintained in the physiological context of the cell. An intriguing observation from our experiments is the dependency of the import process, contrasting with the independency of the export process, on mechanical stability of translocating constructs. This implies that, regardless of any molecular consideration, import is an activated process whereas export is not. These findings are likely to be general, since they were confirmed by the nuclear translocation of two independent experimental approaches, namely the chemical control (serum stimulation) of MRTFA-based constructs and the optical control of the LEXY-based constructs.

In conclusion, our experiments demonstrate that, in addition to protein size[54] and surface properties[53], mechanical stability emerges as an additional intrinsic property of proteins that is capable of regulating their nuclear translocation. From an applied perspective, our findings could be tested *in vitro* using artificial nuclear pore complexes[55], and potentially used in the design of new molecular approaches aimed at externally modifying the mechanical stability of target transcription factors to selectively regulate nuclear localization and gene expression on demand.

Materials and methods

Plasmid constructs and (poly)protein engineering. All genes and reagents were obtained by Thermo Fisher Scientific unless stated otherwise. The full-length MRTFA-GFP vector[11] was kindly provided by Maria Vartiainen, and the pEBFP2-N1 and pEYFP-N1 vectors were kindly provided by Maddy Parsons. pEBFP2-C1, pmCherry-NLS, and pmCherry-RanQ69L were obtained from Addgene. Ig27 mutants were either created by site-directed mutagenesis by PCR or were ordered and subcloned into the pEGFP-MRTFA vector. The Spy0128 pilin domain, Spy0128 E258A mutant, R16 domain of spectrin, Ig27$_{WT}$, and Ig27$_{V11P}$ were cloned using KpnI restriction enzymes. Spy0128 E117A mutant, Ig27$_{V15P}$, Ig27$_{V13P}$, and Ig27$_{Y9P}$ were cloned using SalI and KpnI restriction enzymes. Ig1 was subcloned from pQE80L, using PCR amplification with the addition of SalI and KpnI restriction sites, into MRTFA-GFP. MRTFA-Ig27$_X$-GFP (X = WT, V11P, V13P, V15P, or Y9P) were subcloned into pEBFP2-N1 and pEYFP-N1 between HindIII and KpnI restriction sites by PCR amplification to incorporate an additional glycine residue in the coding sequence in order to remain in reading frame with the fluorescent tag. Ig32 was ordered with SalI and KpnI restriction sites for cloning into pEBFP2-N1 and pEYFP-N1 vectors and also incorporated an additional serine residue. For LEXY optogenetic experiments, the NLS-mCherry-LEXY (pDN122) plasmid was

obtained from Addgene (72655). The Ig27$_{WT}$ and Ig27$_{V13P}$ monomers were amplified using primers designed to add one Gly residue and Gly-Ala residues on the N- and C-termini of the insert, respectively. The amplified fragment was blunt-end ligated into the NLS-mCherry-LEXY plasmid cut with BmgBI between NLS and mCherry. Colonies containing the insert in the correct direction were verified by colony PCR using direction-specific primers. Recombinant plasmids were transformed in XL1Blue (Agilent Technologies) or Top10 (kind gift by Dr. Mark Pfuhl) competent cells. Selected colonies were grown in Luria broth (LB) supplemented with 100 mg/ml kanamycin or ampicillin at 37 °C. Cells were lysed and plasmid DNA was purified prior to transfection using a Qiagen kit according to the manufacturer's instructions. Immunoglobulin monomers for differential scanning fluorimetry (Ig27$_{WT}$, Ig27$_{V11P}$, Ig27$_{V13P}$, Ig27$_{V15P}$, and Ig27$_{Y9P}$) were subcloned into pQE80L vector (Qiagen) between BamHI and KpnI restriction sites. Immunoglobulin polyproteins for single-molecule force spectroscopy, (Ig1–Ig27$_{C47A-C63A}$)$_4$, (Ig27$_{WT}$)$_8$, and (Ig32)$_8$, all containing two additional cysteine residues, were constructed using BamHI, BglII and KpnI restriction sites. Constructs were expressed in *E. coli* BLR(D3) cells (Novagen). Cells were grown in LB supplemented with 100 mg/ml ampicillin at 37 °C. After reaching an OD$_{600}$ of ~0.6, cultures were induced with 1 mM isopropyl-β-D-thiogalactopyranoside and grown at 25 °C for 16 hours. Cells were disrupted by French press and purified by Talon affinity resin (Clontech) using wash buffer (50 mM phosphate buffer, 300 mM NaCl, 20 mM imidazole, pH 7.0) and elution buffer supplemented with 250 mM imidazole. This was followed by gel filtration using a Superdex 200 10/300 GL column (GE Biosciences). Proteins were stored in PBS pH 7.3 at 4 °C.

Cell culture, stable and transient transfection, and drug treatment. U2OS (American Type Culture Collection) and MDA-MB-231 (kindly provided by Maddy Parsons) and HeLa (kindly provided by Ulrike Eggert) cells were grown in complete media – DMEM high glucose (Sigma-Aldrich) supplemented with 10% foetal bovine serum (FBS, Sigma-Aldrich), 100 U/ml penicillin, 100 mg/ml streptomycin, and 2 mM glutamine (Invitrogen). For transient expression, U2OS and MDA-MB-231 cells were transfected with 1 µg of constructs using Fugene (Promega) according to the manufacturer's protocol. U2OS cells stably expressing GFP, MRTFA-GFP, MRTFA-Ig27$_{WT}$-GFP or MRTFA-Ig27$_{V13P}$-GFP were generated by transfection using Fugene, followed by selection with 500 µg/ml geneticin (Thermo Fisher Scientific). After FACS sorting, polyclonal cell lines were obtained and cultured in complete media supplemented with 500 µg/ml geneticin. Cells were starved by withdrawing serum and incubating in serum-starved medium containing 0.3% FBS for 24 hours. Starved cells were stimulated with 15% serum for the indicated time. Where indicated, U2OS cells were treated with 20 nM leptomycin B (Sigma-Aldrich) for 1 hour during live imaging experiments and for 4 hours for cells plated on polyacrylamide gels, 100 nM latrunculin B (Abcam) for 40 minutes, or 40 µM importazole (Abcam) for 1 hour.

Live cell imaging and quantification. Cells transfected with the indicated constructs were seeded and incubated overnight onto glass-bottom dishes. Cells were then serum starved for 24 hours. For live imaging acquisition, cells were stimulated with 15% FBS or treated with the drugs indicated. Images were acquired with a Nikon A1R confocal microscope with a 60X NA 1.40 oil objective and laser and emission filter wavelengths of 405 nm and 450/50 nm respectively for BFP, 488.2 nm and 540/30 nm respectively for GFP and YFP, and

561.9nm and 595/50 nm respectively for mCherry. The microscope was operated with the Nikon Perfect Focus System and controlled by NIS Elements software. Images were typically acquired every 30 seconds during 30 or 60 minutes. The microscope was enclosed in a Solent Scientific environmental chamber with temperature and CO_2 control. Live cell images were processed to quantify MRTFA localisation using a custom-made MATLAB (MathWorks) script. First, the background was measured and subtracted. Next, the outlines of the whole cell and the nucleus were defined by the user to determine the total fluorescent intensities of the cell and nucleus. The nuclear intensity was divided by the cell intensity to provide a measure of the nuclear MRTFA fraction. This procedure was repeated for all frames in an imaging sequence to obtain the time-dependent behaviour of the nuclear MRTFA fraction. **Kinetic analysis.** For each stimulated cell, the time-dependence of the nuclear MRTFA fraction, $n(t)$, is fit to

$$n(t) = n_0 e^{-kt} + n_e(1 - e^{-kt})$$

where n_0 and n_e are the initial and equilibrium nuclear MRTFA fractions respectively, and k is the total rate constant (for simplicity we refer to n_e as the equilibrium accumulation). For data from a stimulated cell to be considered 'good', its behaviour must obey the criteria $0 \leq n_0 \leq n_e \leq 1$ and $k \geq 1/T$ where T is the duration over which observations are made. In practice, this entails that cells that (i) do not respond to serum stimulation, (ii) exhibit very slow nuclear accumulation (do not display plateauing behaviour and thus provide unreliable information regarding export), or (iii) have artefacts (e.g. discontinuities) in their nuclear accumulation curves due to unavoidable technical reasons (such as sudden changes of shape and cell death), are not considered for kinetic analysis. For U2OS cells, $t = 0$ is defined as 2 minutes after serum stimulation, such that the initial transient behaviour (before stimulation is fully activated) is not fitted. For MDA-MB-231 cells, which respond slower to serum, the definition of $t = 0$ rises to 5 minutes after stimulation. For the optogenetic experiments, $t = 0$ coincides with cessation of illumination since conformational relaxation of LOV domains occurs on a rapid timescale relative to our experiments. Before averaging the time courses of individual cells for a given condition, any variations in n_0 between cells (which is not of interest) must be corrected for in a way that does not alter n_e or k (which are of interest). This correction is performed by subtracting $n_0 e^{-kt}$ from the nuclear MRTFA fraction data to give a corrected nuclear MRTFA fraction, $\tilde{n}(t)$. Assuming pseudo-first-order behaviour (see supplementary information), an equivalent mathematical description of the translocation kinetics is given by import and export rate constants, k_I and k_E respectively, which relate to the equilibrium accumulation and total rate constant via $n_e = k_I/(k_I + k_E)$ and $k = k_I + k_E$. As such, there are two equivalent fittings to the corrected nuclear MRTFA fraction:

$$\tilde{n}(t) = n_e(1 - e^{-kt}) = \frac{k_I}{k_I + k_E}\left(1 - e^{-(k_I+k_E)t}\right)$$

Final values of these parameters-of-interest are obtained from the fitting of averaged time courses. Errors in these values are given by the standard error of fitting parameters obtained from the fitting of the time courses from individual cells.

Fluorescence Loss in Photobleaching (FLIP). U2OS cells transfected with either MRTFA-Ig27$_{WT}$-GFP or MRTFA-Ig27$_{V13P}$-GFP were seeded and incubated overnight onto glass-

bottom dishes. Cells were serum-starved for 24 hours and then stimulated for 30 minutes with 15% serum. Imaging (4% laser power) and photobleaching (60% laser power) were performed using the same 488.2 nm laser. Two images were acquired, followed by repeated photobleaching scanning for 40 seconds in a 30 µm × 30 µm cytoplasmic region. After photobleaching, images were acquired every second for 180 seconds. From the acquired images, the decay in MRTFA nuclear intensity was measured as described above. To negate the effects of unintended photobleaching during post-photobleaching imaging, the decay in nuclear intensity was corrected using the fluorescent intensity decrease of a nearby reference cell. Finally, nuclear MRTFA intensity values were normalised relative to the intensity measured immediately after photobleaching.

Optogenetic control of nuclear export. Activation and imaging of NLS-Ig27$_{WT}$-mCherry-LEXY (and NLS-Ig27$_{V13P}$-mCherry-LEXY) was performed with laser wavelengths 488.2 nm and 561.9 nm, respectively. mCherry images were acquired every 30 seconds for the entirety of the data acquisition. After 1 minute, prior to each mCherry image, cells were irradiated with the blue laser to expose the NES of LEXY, this was repeated for 10 minutes. For the remaining 20 minutes of data acquisition – the dark state recovery – only mCherry imaging took place. Kinetic analysis of the dark state recovery was performed in the same way (described above) as for serum-stimulation cells.

Single molecule force spectroscopy. Single molecule force spectroscopy experiments were conducted using both a home-made and a Luigs and Neumann force spectrometer operating at room temperature, as described previously[56]. Samples were prepared by depositing 0.5–5 µl of protein (at a concentration of 1–5 mg/ml in PBS pH 7.3) onto a gold-coated cover slide which had been plasma cleaned for 10 minutes prior to deposition. Each cantilever (MLCT-C, Bruker) was calibrated using the equipartition theorem, giving a typical spring constant of ~12–18 pN/nm. To stretch an individual protein, the cantilever tip was first pushed against the surface at high force (~2 nN) to promote non-specific adhesion between the protein and the tip. The tethered protein was subsequently pulled by retracting the cantilever at a constant velocity of 400 nm/s relative to the substrate. All data was recorded and analysed using custom-written software in Igor Pro (WaveMetrics). For the octameric polyproteins (Ig27$_{WT}$)$_8$ and (Ig32)$_8$, only traces showing the signature of at least 5 unfolding events were selected for analysis. For the tetrameric chimera polyprotein (Ig1–Ig27$_{C47A-C63A}$)$_4$ only trajectories displaying at least 2 Ig27$_{C47A-C63A}$ unfolding events (hallmarked by an increment of ~28 nm at ~200 pN) were analysed. There is no significant difference between the unfolding forces of Ig27$_{WT}$ and Ig27$_{C47A-C63A}$ (Fig. S5). Each protein unfolding event was fitted with the worm-like chain (WLC) model of polymer elasticity to obtain the increment in contour length.

Differential scanning fluorimetry. Differential scanning fluorimetry (DSF) experiments[57] were performed to find the melting temperatures of Ig27 mutants (Ig27$_{V13P}$, Ig27$_{V11P}$, Ig27$_{V15P}$, Ig27$_{WT}$, and Ig27$_{Y9P}$) using a Stratagene Mx3005P Real-Time (RT) qPCR System. The process of thermally-induced unfolding was monitored by measuring the fluorescence of SYPRO Orange dye (Thermo Fisher Scientific) with the excitation and emission wavelengths of 587 nm and 607 nm respectively. Data were collected at 1 °C intervals from 25 °C through to 95 °C with a heating rate of 1 °C/min. Preliminary tests were carried out to find the optimal combination of protein concertation (Ig27$_{WT}$ used) and dye dilution. At the

recommended concentrations, the fluorescence signal increase, which accompanied thermally-induced unfolding, was too low to produce reliable results. This was due to the small nature of Ig domains in question, and thus the sparsity of hydrophobic residues (to which the dye binds to become fluorescent) being exposed upon unfolding. An optimal signal-to-noise ratio was achieved with a 50 µM protein concentration and 1:500 dye dilution in 50 mM PBS pH 7.3 with 300 mM NaCl. As such, for each protein, 240 µl of 100 µM protein and 240 µl of 1:250 diluted dye were mixed and aliquoted into 12 wells (40 µl per well) of a 96-well, non-skirted, low-profile, 0.2 ml PCR plate (Thermo Fisher Scientific), sealed with an optical adhesive cover (Applied Biosystems). As such, for each Ig27 mutant, 12 DSF melting curves were obtained under identical conditions. To find the melting temperature of a given Ig27 mutant, each individual curve was fit to a sigmoidal function between its minimum and maximum fluorescence values and the temperature at the sigmoid midpoint was taken as the melting temperature for that curve. The quoted melting temperature is then the mean ± s.e.m. from these 12 measurements. For a given Ig27 mutant, averaged DSF melting curves were obtained after normalising each individual curve by setting the area under the curve to unity [57].

Western blotting. Cells were lysed using radioimmunoprecipitation assay (RIPA) buffer with a protease inhibitor cocktail. Lysates were separated by SDS-PAGE and transferred to a polyvinylidene difluoride membrane. Membranes were incubated in blocking buffer (3% BSA in PBS containing 0.1% Tween-20) for 1 hour at room temperature and then incubated overnight with the following antibodies: MRTFA (Santa Cruz) and GAPDH (GeneTex). Antibodies were visualized using the ECL detection system (Bio-Rad). Densitometric analysis was performed using ImageJ.

RNA extraction and RT qPCR. RNA from U2OS cells was extracted on ice using RNeasy Mini kit (Qiagen) according to the manufacturer's instructions and treated with DNase (Invitrogen). RNA concentration was determined, and purity was checked, by measuring the A_{260}/A_{280} ratio. Relative mRNA expression of genes was determined by RT qPCR assay using SYBR-Green detection chemistry (Agilent) and the ViiA7 RT qPCR System (Applied Biosystems). Primers used were MYL9 CATCCATGAGGACCACCTCCG/CTGGGGTGGCCTAGTCGTC[6], ACTB (QT00095431, Qiagen) and SRF (QT00084063, Qiagen). Relative abundances of template cDNA were calculated by the comparative CT (ΔΔCT) method. Each sample was normalized to the level of a GAPDH (PPH00150F-200 qPCR, Qiagen).

Wound healing assay. U2OS cells stably expressing a GFP empty vector, MRTFA-GFP, MRTFA-Ig27$_{WT}$-GFP, or MRTFA-Ig27$_{V13P}$-GFP were seeded onto 6-well plates and incubated overnight at 37 °C. After reaching 80% confluence, cells were first serum starved for 24 hours and then stimulated with 10% serum for other 24 hours. Scratch wounds were made by scraping a 10 µl pipette tip across each cell layer[58]. For each condition regions were imaged at time zero, to record the initial area of the wounds, and at 24 hours, using a Nikon Ti2 microscope with a 10x NA 0.3 and a Nikon DS-Qi2 camera, controlled by NIS Elements software. Wound recovery was calculated by measuring the change in the wound area from time zero to 24 hours. These areas were user-defined in ImageJ. Experiments were performed independently three times, evaluating eight regions within each scratch. Final values are normalised with respect to MRTFA-GFP.

Random migration assay. MDA-MB-231 transiently transfected with a GFP empty vector, MRTFA-GFP, MRTFA-Ig27$_{WT}$-GFP, or MRTFA-Ig27$_{V13P}$-GFP, were plated on FN-coated 6-well plates in serum-starved medium for 16 hours and the stimulated with 10% serum for other 24 hours. Cells were then imaged using a Nikon Ti2 microscope with a 10x NA 0.3 and a Nikon DS-Qi2 camera, controlled by NIS Elements software. In order to visualize and track successfully transfected cells, a GFP fluorescence image was acquired at time zero. Bright field images were then acquired every 5 minutes for 13 hours. Cells were tracked, and their migration speed was determined using the Manual Tracking plug-in for ImageJ.

Author contributions. S.G.-M. conceived the research. E.I. designed and performed cell biology, live-cell imaging experiments, motility assays and qPCR experiments. A.S. designed and performed live-cell imaging analysis and kinetic modelling. P.R-L., S.J.B., E.R. and A.L. performed molecular biology work. A.E.M.B. and Y.J.W. conducted single molecule nanomechanical experiments and A.E.M.B analysed data. E.R. with A.S. conducted and analysed differential scanning fluorimetry experiments. S.G.B., F.P. and V.S.R acquired preliminary data. C.M.S. and P.R-C. participated in data discussion. S.G.-M., E.I. and A.S. wrote the paper.

Competing financial interests. The authors declare no competing financial interests.

Data availability. Data supporting this research can be obtained from the corresponding author upon reasonable request.

References
1   Vogel, V. & Sheetz, M. Local force and geometry sensing regulate cell functions. *Nat Rev Mol Cell Biol* **7**, 265-275, doi:10.1038/nrm1890 (2006).
2   Dupont, S. *et al.* Role of YAP/TAZ in mechanotransduction. *Nature* **474**, 179-183, doi:10.1038/nature10137 (2011).

3   Markiewicz, E. *et al.* The inner nuclear membrane protein emerin regulates beta-catenin activity by restricting its accumulation in the nucleus. *EMBO J* **25**, 3275-3285, doi:10.1038/sj.emboj.7601230 (2006).

4   Moon, H. S., Even-Ram, S., Kleinman, H. K. & Cha, H. J. Zyxin is upregulated in the nucleus by thymosin beta4 in SiHa cells. *Exp Cell Res* **312**, 3425-3431, doi:10.1016/j.yexcr.2006.07.021 (2006).

5   Fedorchak, G. R., Kaminski, A. & Lammerding, J. Cellular mechanosensing: getting to the nucleus of it all. *Prog Biophys Mol Biol* **115**, 76-92, doi:10.1016/j.pbiomolbio.2014.06.009 (2014).

6   Medjkane, S., Perez-Sanchez, C., Gaggioli, C., Sahai, E. & Treisman, R. Myocardin-related transcription factors and SRF are required for cytoskeletal dynamics and experimental metastasis. *Nat Cell Biol* **11**, 257-268, doi:10.1038/ncb1833 (2009).

7   Olson, E. N. & Nordheim, A. Linking actin dynamics and gene transcription to drive cellular motile functions. *Nat Rev Mol Cell Biol* **11**, 353-365, doi:10.1038/nrm2890 (2010).

8   Jain, N., Iyer, K. V., Kumar, A. & Shivashankar, G. V. Cell geometric constraints induce modular gene-expression patterns via redistribution of HDAC3 regulated by actomyosin contractility. *Proc Natl Acad Sci U S A* **110**, 11349-11354, doi:10.1073/pnas.1300801110 (2013).

9   Connelly, J. T. *et al.* Actin and serum response factor transduce physical cues from the microenvironment to regulate epidermal stem cell fate decisions. *Nat Cell Biol* **12**, 711-718, doi:10.1038/ncb2074 (2010).

10   Miralles, F., Posern, G., Zaromytidou, A. I. & Treisman, R. Actin dynamics control SRF activity by regulation of its coactivator MAL. *Cell* **113**, 329-342 (2003).

11   Ho, C. Y., Jaalouk, D. E., Vartiainen, M. K. & Lammerding, J. Lamin A/C and emerin regulate MKL1-SRF activity by modulating actin dynamics. *Nature* **497**, 507-511, doi:10.1038/nature12105 (2013).

12   Pawlowski, R., Rajakyla, E. K., Vartiainen, M. K. & Treisman, R. An actin-regulated importin alpha/beta-dependent extended bipartite NLS directs nuclear import of MRTF-A. *EMBO J* **29**, 3448-3458, doi:10.1038/emboj.2010.216 (2010).

13   Mouilleron, S., Langer, C. A., Guettler, S., McDonald, N. Q. & Treisman, R. Structure of a pentavalent G-actin*MRTF-A complex reveals how G-actin controls nucleocytoplasmic shuttling of a transcriptional coactivator. *Sci Signal* **4**, ra40, doi:10.1126/scisignal.2001750 (2011).

14   Vartiainen, M. K., Guettler, S., Larijani, B. & Treisman, R. Nuclear actin regulates dynamic subcellular localization and activity of the SRF cofactor MAL. *Science* **316**, 1749-1752, doi:10.1126/science.1141084 (2007).

15   Baarlink, C., Wang, H. & Grosse, R. Nuclear actin network assembly by formins regulates the SRF coactivator MAL. *Science* **340**, 864-867, doi:10.1126/science.1235038 (2013).

16   Kim, S. J. *et al.* Integrative structure and functional anatomy of a nuclear pore complex. *Nature* **555**, 475-482, doi:10.1038/nature26003 (2018).

17   Maillard, R. A. *et al.* ClpX(P) generates mechanical force to unfold and translocate its protein substrates. *Cell* **145**, 459-469, doi:10.1016/j.cell.2011.04.010 (2011).

18   Olivares, A. O., Kotamarthi, H. C., Stein, B. J., Sauer, R. T. & Baker, T. A. Effect of directional pulling on mechanical protein degradation by ATP-dependent proteolytic machines. *Proc Natl Acad Sci U S A*, doi:10.1073/pnas.1707794114 (2017).

19   Rodriguez-Larrea, D. & Bayley, H. Multistep protein unfolding during nanopore translocation. *Nat Nanotechnol* **8**, 288-295, doi:10.1038/nnano.2013.22 (2013).

20   Maimon, T., Elad, N., Dahan, I. & Medalia, O. The human nuclear pore complex as revealed by cryo-electron tomography. *Structure* **20**, 998-1006, doi:10.1016/j.str.2012.03.025 (2012).

21   Lin, D. H. *et al.* Architecture of the symmetric core of the nuclear pore. *Science* **352**, aaf1015, doi:10.1126/science.aaf1015 (2016).

22   Lemke, E. A. The Multiple Faces of Disordered Nucleoporins. *J Mol Biol* **428**, 2011-2024, doi:10.1016/j.jmb.2016.01.002 (2016).

23   Grunwald, D. & Singer, R. H. Multiscale dynamics in nucleocytoplasmic transport. *Curr Opin Cell Biol* **24**, 100-106, doi:10.1016/j.ceb.2011.11.011 (2012).

24   Schmidt, H. B. & Gorlich, D. Transport Selectivity of Nuclear Pores, Phase Separation, and Membraneless Organelles. *Trends Biochem Sci* **41**, 46-61, doi:10.1016/j.tibs.2015.11.001 (2016).

25   Rout, M. P., Aitchison, J. D., Magnasco, M. O. & Chait, B. T. Virtual gating and nuclear transport: the hole picture. *Trends Cell Biol* **13**, 622-628 (2003).

26   Lim, R. Y. *et al.* Nanomechanical basis of selective gating by the nuclear pore complex. *Science* **318**, 640-643, doi:10.1126/science.1145980 (2007).

27   Frey, S., Richter, R. P. & Gorlich, D. FG-rich repeats of nuclear pore proteins form a three-dimensional meshwork with hydrogel-like properties. *Science* **314**, 815-817, doi:10.1126/science.1132516 (2006).

28   Yamada, J. *et al.* A bimodal distribution of two distinct categories of intrinsically disordered structures with separate functions in FG nucleoporins. *Mol Cell Proteomics* **9**, 2205-2224, doi:10.1074/mcp.M000035-MCP201 (2010).

29   Peters, R. Translocation through the nuclear pore complex: selectivity and speed by reduction-of-dimensionality. *Traffic* **6**, 421-427, doi:10.1111/j.1600-0854.2005.00287.x (2005).

30   Lim, R. Y. *et al.* Flexible phenylalanine-glycine nucleoporins as entropic barriers to nucleocytoplasmic transport. *Proc Natl Acad Sci U S A* **103**, 9512-9517, doi:10.1073/pnas.0603521103 (2006).

31   Fisher, T. E., Oberhauser, A. F., Carrion-Vazquez, M., Marszalek, P. E. & Fernandez, J. M. The study of protein mechanics with the atomic force microscope. *Trends Biochem Sci* **24**, 379-384 (1999).

32   Mehlin, H., Daneholt, B. & Skoglund, U. Translocation of a specific premessenger ribonucleoprotein particle through the nuclear pore studied with electron microscope tomography. *Cell* **69**, 605-613 (1992).

33   Grunwald, D. & Singer, R. H. In vivo imaging of labelled endogenous beta-actin mRNA during nucleocytoplasmic transport. *Nature* **467**, 604-607, doi:10.1038/nature09438 (2010).

34   Stevens, B. J. & Swift, H. RNA transport from nucleus to cytoplasm in Chironomus salivary glands. *J Cell Biol* **31**, 55-77 (1966).

35   Lowe, A. R. *et al.* Selectivity mechanism of the nuclear pore complex characterized by single cargo tracking. *Nature* **467**, 600-603, doi:10.1038/nature09285 (2010).

36   Elosegui-Artola, A. *et al.* Force Triggers YAP Nuclear Entry by Regulating Transport across Nuclear Pores. *Cell* **171**, 1397-1410 e1314, doi:10.1016/j.cell.2017.10.008 (2017).

37   Kudo, N. *et al.* Leptomycin B inhibition of signal-mediated nuclear export by direct binding to CRM1. *Exp Cell Res* **242**, 540-547, doi:10.1006/excr.1998.4136 (1998).

38   Li, H., Carrion-Vazquez, M., Oberhauser, A. F., Marszalek, P. E. & Fernandez, J. M. Point mutations alter the mechanical stability of immunoglobulin modules. *Nat Struct Biol* **7**, 1117-1120, doi:10.1038/81964 (2000).

39   Kang, H. J., Coulibaly, F., Clow, F., Proft, T. & Baker, E. N. Stabilizing isopeptide bonds revealed in gram-positive bacterial pilus structure. *Science* **318**, 1625-1628, doi:10.1126/science.1145806 (2007).

40   Alegre-Cebollada, J., Badilla, C. L. & Fernandez, J. M. Isopeptide bonds block the mechanical extension of pili in pathogenic Streptococcus pyogenes. *J Biol Chem* **285**, 11235-11242, doi:10.1074/jbc.M110.102962 (2010).

41   Kang, H. J. & Baker, E. N. Intramolecular isopeptide bonds give thermodynamic and proteolytic stability to the major pilin protein of Streptococcus pyogenes. *J Biol Chem* **284**, 20729-20737, doi:10.1074/jbc.M109.014514 (2009).

42   Li, H. *et al.* Reverse engineering of the giant muscle protein titin. *Nature* **418**, 998-1002, doi:10.1038/nature00938 (2002).

43   Li, H. & Fernandez, J. M. Mechanical design of the first proximal Ig domain of human cardiac titin revealed by single molecule force spectroscopy. *J Mol Biol* **334**, 75-86 (2003).

44   Carrion-Vazquez, M. *et al.* Mechanical and chemical unfolding of a single protein: a comparison. *Proc Natl Acad Sci U S A* **96**, 3694-3699 (1999).

45   Randles, L. G., Rounsevell, R. W. & Clarke, J. Spectrin domains lose cooperativity in forced unfolding. *Biophys J* **92**, 571-577, doi:10.1529/biophysj.106.093690 (2007).

46   Perez-Jimenez, R., Garcia-Manyes, S., Ainavarapu, S. R. & Fernandez, J. M. Mechanical unfolding pathways of the enhanced yellow fluorescent protein revealed by single molecule force spectroscopy. *J Biol Chem* **281**, 40010-40014, doi:10.1074/jbc.M609890200 (2006).

47   Soderholm, J. F. *et al.* Importazole, a small molecule inhibitor of the transport receptor importin-beta. *ACS Chem Biol* **6**, 700-708, doi:10.1021/cb2000296 (2011).

48   Niopek, D., Wehler, P., Roensch, J., Eils, R. & Di Ventura, B. Optogenetic control of nuclear protein export. *Nat Commun* **7**, 10624, doi:10.1038/ncomms10624 (2016).

49   Record, J. *et al.* Immunodeficiency and severe susceptibility to bacterial infection associated with a loss-of-function homozygous mutation of MKL1. *Blood* **126**, 1527-1535, doi:10.1182/blood-2014-12-611012 (2015).

50   Beck, M. & Hurt, E. The nuclear pore complex: understanding its function through structural insight. *Nat Rev Mol Cell Biol* **18**, 73-89, doi:10.1038/nrm.2016.147 (2017).

51 von Appen, A. *et al.* In situ structural analysis of the human nuclear pore complex. *Nature* **526**, 140-143, doi:10.1038/nature15381 (2015).

52 Bestembayeva, A. *et al.* Nanoscale stiffness topography reveals structure and mechanics of the transport barrier in intact nuclear pore complexes. *Nat Nanotechnol* **10**, 60-64, doi:10.1038/nnano.2014.262 (2015).

53 Frey, S. *et al.* Surface Properties Determining Passage Rates of Proteins through Nuclear Pores. *Cell* **174**, 202-217 e209, doi:10.1016/j.cell.2018.05.045 (2018).

54 Mohr, D., Frey, S., Fischer, T., Guttler, T. & Gorlich, D. Characterisation of the passive permeability barrier of nuclear pore complexes. *EMBO J* **28**, 2541-2553, doi:10.1038/emboj.2009.200 (2009).

55 Ketterer, P. *et al.* DNA origami scaffold for studying intrinsically disordered proteins of the nuclear pore complex. *Nat Commun* **9**, 902, doi:10.1038/s41467-018-03313-w (2018).

56 Popa, I., Kosuri, P., Alegre-Cebollada, J., Garcia-Manyes, S. & Fernandez, J. M. Force dependency of biochemical reactions measured by single-molecule force-clamp spectroscopy. *Nat Protoc* **8**, 1261-1276, doi:10.1038/nprot.2013.056 (2013).

57 Rosa, N. *et al.* Meltdown: A Tool to Help in the Interpretation of Thermal Melt Curves Acquired by Differential Scanning Fluorimetry. *J Biomol Screen* **20**, 898-905, doi:10.1177/1087057115584059 (2015).

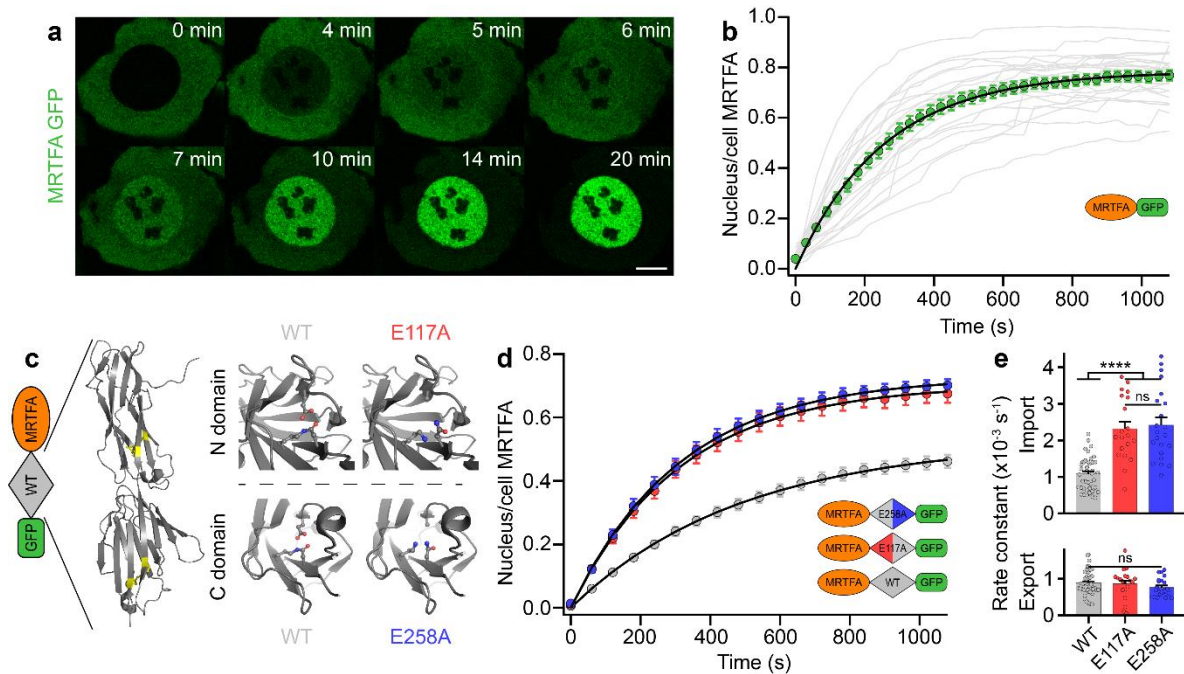58 Rodriguez, L. G., Wu, X. & Guan, J. L. Wound-healing assay. *Methods Mol Biol* **294**, 23-29 (2005).

Figure 1. Protein unfolding modulates the kinetics of nuclear import. (a) Representative confocal image gallery showing MRTFA nuclear translocation, upon serum stimulation, in a U2OS cell expressing MRTFA-GFP. 10µm scale bar. **(b)** Individual (light grey lines) and averaged (green points, mean ± s.e.m.) time courses of nucleus/cell MRTFA. These translocation dynamics can be fit to $n(t) = n_\mathrm{e}(1 - e^{-kt})$ (black line), yielding an equilibrium accumulation n_e = 0.784±0.019 and a total rate constant k = 3.91±0.42 ×10^{-3} s^{-1}, which can be decomposed into import and export rate constants k_I = 3.07±0.32 ×10^{-3} s^{-1} and k_E = 0.84±0.14 ×10^{-3} s^{-1}, respectively. Data are from four independent experiments (n = 24). **(c)** Schematic representation of the MRTFA-GFP construct concatenated with Spy0128$_\mathrm{WT}$, the latter comprised of two domains each containing an isopeptide bond close to their termini. Point mutations (E117A, N-terminal domain) or (E258A, C-terminal domain) abrogate isopeptide bond formation, enabling domain unfolding. **(d)** Averaged (mean ± s.e.m.) time courses of nucleus/cell MRTFA in U2OS cells expressing MRTFA-Spy0128$_\mathrm{WT}$-GFP, MRTFA-Spy0128$_\mathrm{E117A}$-GFP, or MRTFA-Spy0128$_\mathrm{E258A}$-GFP, after serum stimulation. Inhibiting isopeptide bond formation clearly increases the rate and extent of MRTFA nuclear translocation. Data are from three independent experiments (WT, n = 41; E117A, n = 20, E258A, n = 22). **(e)** The kinetics of nuclear translocation of MRTFA-Spy0128$_\mathrm{WT}$-GFP exhibits a slow nuclear import (k_I = 1.08±0.07 ×10^{-3} s^{-1}) compared to the faster E117A and E258A mutants (k_I = 2.32±0.19 ×10^{-3} s^{-1} and k_I = 2.42±0.21 ×10^{-3} s^{-1}, respectively). While both E117A and E258A mutants significantly increase the import rate constant, export is not significantly varied. Two-tailed t-tests, ns P > 0.05 and **** $P \leq 0.0001$.
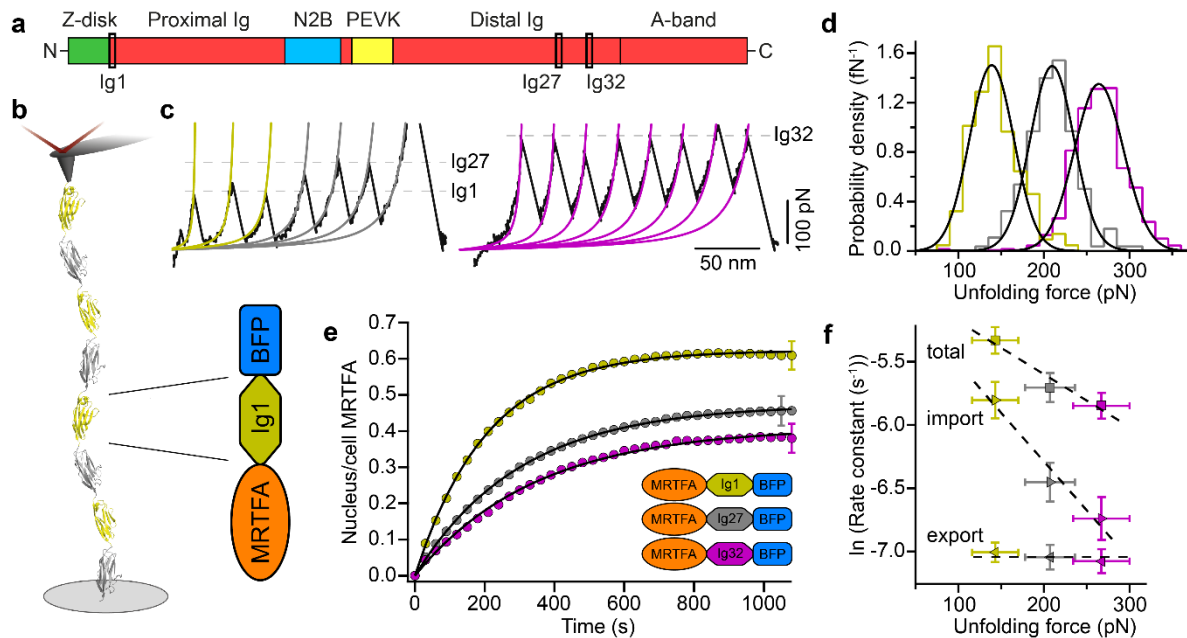
Figure 2. The kinetics of MRTFA nuclear import is regulated by its mechanical properties. **(a)** Structural schematic of titin, showing the distribution of selected Ig domains along the N-C termini direction. **(b)** Schematics of a single molecule force spectroscopy experiment, whereby a polyprotein made of selected titin Ig domains is tethered between an AFM cantilever tip and a gold substrate. Inserting Ig domains within MRTFA constructs enables one to probe the effect of mechanical stability on nuclear translocation. **(c)** Stretching individual (Ig1-Ig27$_{C47A-C63A}$)$_4$, (Ig27)$_8$ and (Ig32)$_8$ polyproteins at a constant velocity of 400 nm s^{-1} gives rise to unfolding trajectories exhibiting saw-tooth patterns, where each force peak corresponds to the unfolding of an individual Ig domain within the polyprotein chain (Fig. S5). **(d)** Probability density histograms of unfolding forces for Ig1 (yellow), Ig27 (grey), and Ig32 (magenta) domains with the associated Gaussian probability density distributions (black) overlaid (unfolding force mean ± s.d.: Ig1, 144±27 pN, n = 137; Ig27, 208±28 pN, n = 186; Ig32, 267±33 pN, n = 936). **(e)** Averaged (mean ± s.e.m.) time courses of nucleus/cell MRTFA in U2OS cells expressing MRTFA-Ig1-BFP, MRTFA-Ig27-BFP, or MRTFA-Ig32-BFP, after serum stimulation. The rate and extent of MRTFA nuclear translocation of the mechanically-labile Ig1 is higher than that of Ig27 and of the mechanically-stable Ig32. Data are from four independent experiments (Ig1, n = 34; Ig27, n = 37, Ig32, n = 44), only a representative error bar is shown per condition. **(f)** Total (squares), import (right-pointing triangles), and export (left-pointing triangles, offset vertically by -0.7 for clarity) rate constants associated with the nuclear translocation of Ig-domain-tagged MRTFA constructs plot against the mechanical stability (unfolding force) of the tagging Ig domain. The import rate constant displays exponential dependence (R^2 = 0.999) with mechanical stability. By contrast, the export rate constant is largely independent of mechanical stability. Rate constants correspond to the fitting parameters from the averaged time courses in (h), associated error bars correspond to the s.e.m. of fitting parameters of the individual time courses. The unfolding forces correspond to the mean ± s.d. of unfolding forces as in (d). Dashed lines are a weighted linear fit (import) and average (export).
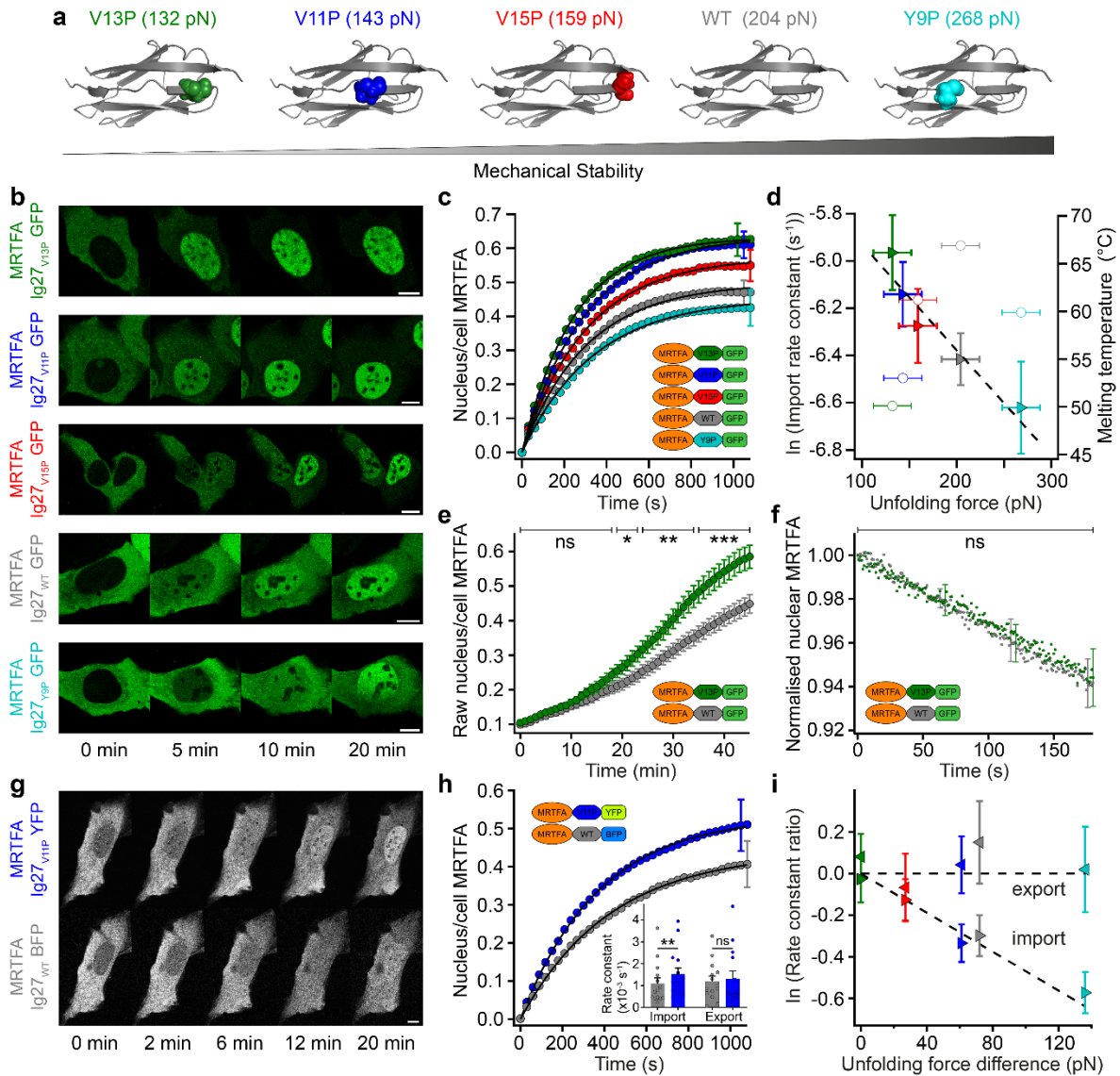
Figure 3. The nuclear pore complex is highly mechanoselective. (a) Selective introduction of point mutations in key residues in the mechanical-clamp region of the Ig27 structure result in subtle changes to its mechanical stability, in the order V13P < V11P < V15P < WT < Y9P, as measured elsewhere by single molecule force spectroscopy experiments[38]. **(b)** Representative confocal image galleries showing MRTFA nuclear translocation, upon serum stimulation, of U2OS cells expressing MRTFA-Ig27$_X$-GFP constructs containing an Ig27 mutant (in order of mechanical stability, top to bottom: V13P, V11P, V15P, WT, Y9P). All scale bars are 10 μm**. (c)** Averaged (mean ± s.e.m.) time courses of MRTFA nuclear translocation, upon serum stimulation, in U2OS cells expressing MRTFA-GFP tagged with different Ig27 mutants – the rate and extent of MRTFA nuclear accumulation is dependent on the tagging Ig27 variant. Data are from two (V11P, n = 26) or three (V13P, n = 22; V15P, n = 25; WT, n = 30; Y9P, n = 17) independent experiments, only a representative error bar is shown per condition. **(d)** The import rate constant (triangles) displays an exponential dependence (dashed line, linear fit, R^2 = 0.988) with the mechanical stability of the tagging

22

Ig27 mutant. By contrast, a weaker correlation is observed with their thermodynamic stability (circles), measured using differential scanning fluorimetry. Import rate constants correspond to the fitting parameters from averaged time courses, associated error bars correspond to the s.e.m. of fitting parameters from individual time courses. Melting temperatures correspond to the mean of 12 replicates (with associated s.e.m. < 0.1 °C for each mutant, Fig. S11). Unfolding forces correspond to the mean ± estimated s.d. (20 pN)[38] as in (a). **(e)** Averaged (mean ± s.e.m.) nuclear accumulation of MRTFA-Ig27$_{V13P}$-GFP and MRTFA-Ig27$_{WT}$-GFP in serum-starved U2OS cells following treatment with leptomycin B. Significantly greater nuclear accumulation of the V13P construct, compared to the WT construct, develops over time (unpaired *t*-test). Data are from three independent experiments (V13P, *n* = 40; WT, *n* = 50). **(f)** Averaged (mean ± s.e.m.) normalised decay of nuclear MRTFA measured in FLIP experiments. The decay in nuclear fluorescent intensity at early times (which isolates the nuclear export process) for MRTFA-Ig27$_{V13P}$-GFP and MRTFA-Ig27$_{WT}$-GFP displays no significant differences at any time (unpaired *t*-test). Data are from three independent experiments (V13P, *n* = 20; WT, *n* = 15). **(g)** Representative confocal image galleries showing MRTFA nuclear translocation, following serum stimulation, of a U2OS cell co-expressing MRTFA-I27$_{WT}$-BFP and MRTFA-I27$_{V11P}$-YFP. 10 µm scale bar. **(h)** Corresponding averaged (mean ± s.e.m.) time courses showing that, within the same cell, the rate and extent of nuclear accumulation of MRTFA tagged with the mechanically-labile Ig27$_{V11P}$ is higher than MRTFA tagged with the mechanically-stable Ig27$_{WT}$. Analysis of the coupled kinetic parameters – the import (or export) rate constants of both constructs within the same cell – display significant differences in terms of import, but not export (inset, paired *t*-test). Data are from four independent experiments (*n* = 14), only a representative error bar is shown per condition. **(i)** Ratios (mean ± s.e.m.) of import (right-pointing triangles) and export (left-pointing triangles) rate constants plot against the unfolding force differences for co-expression experiments (full details in Fig. S14). Data are from four (WT/V11P) or three (all other) independent experiments (left to right, BFP/YFP: V13P/V13P, *n* = 9; V15P/V13P, *n* = 8; WT/V11P, *n* = 14; WT/V13P, *n* = 15; Y9P/V13P, *n* = 12). Ratios correspond to the mean ± s.e.m. of the ratios of the fitting parameters associated with translocation of the BFP construct, with respect to the YFP construct, from each individual cell. Dashed lines are a weighted linear fit (import) and average (export). Significance levels for two tailed *t*-tests, ns *P* > 0.05, * *P* ≤ 0.05, ** *P* ≤ 0.01, and *** *P* ≤ 0.001.
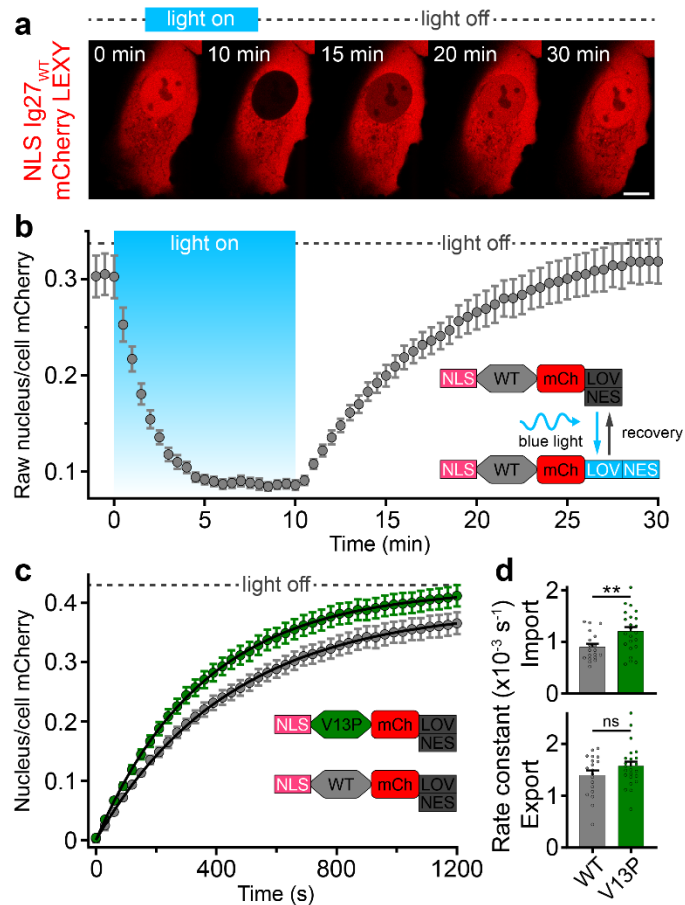
Figure 4. The mechanical selectivity of the NPC probed with optogenetic constructs. (a) Representative confocal image gallery of a U2OS cell expressing NLS-Ig27$_{WT}$-mCherry-LEXY showing that nuclear localisation of this construct can be controlled by illumination with blue light. **(b)** Averaged (mean ± s.e.m.) raw time courses of nuclear localization of NLS-Ig27$_{WT}$-mCherry-LEXY. In the dark state, the NES of LEXY is docked with the LOV domain (inset), and nuclear localization is observed. Upon illumination, the LOV domain undergoes a conformational change that exposes the NES motif, resulting in the fast exclusion of the construct from the nucleus. Nuclear localisation is recovered over time when the illumination is removed (dark state recovery). Data are from three independent experiments (*n* = 19). **(c)** Averaged (mean ± s.e.m.) time courses of dark-state-recovery nuclear localization of NLS-Ig27$_{V13P}$-mCherry-LEXY and NLS-Ig27$_{WT}$-mCherry-LEXY. Data are from three independent experiments (V13P, *n* = 23). (**d**) The nuclear import rate constant of the V13P construct (k_I = 1.20±0.08 ×10^{-3} s^{-1}) was significantly higher than the WT construct (k_I = 0.900±0.063 ×10^{-3} s^{-1}). By contrast, no statistically significant difference was found for the export rate constant. Two-tailed *t*-tests, ns *P* > 0.05 and ** *P* ≤ 0.01.
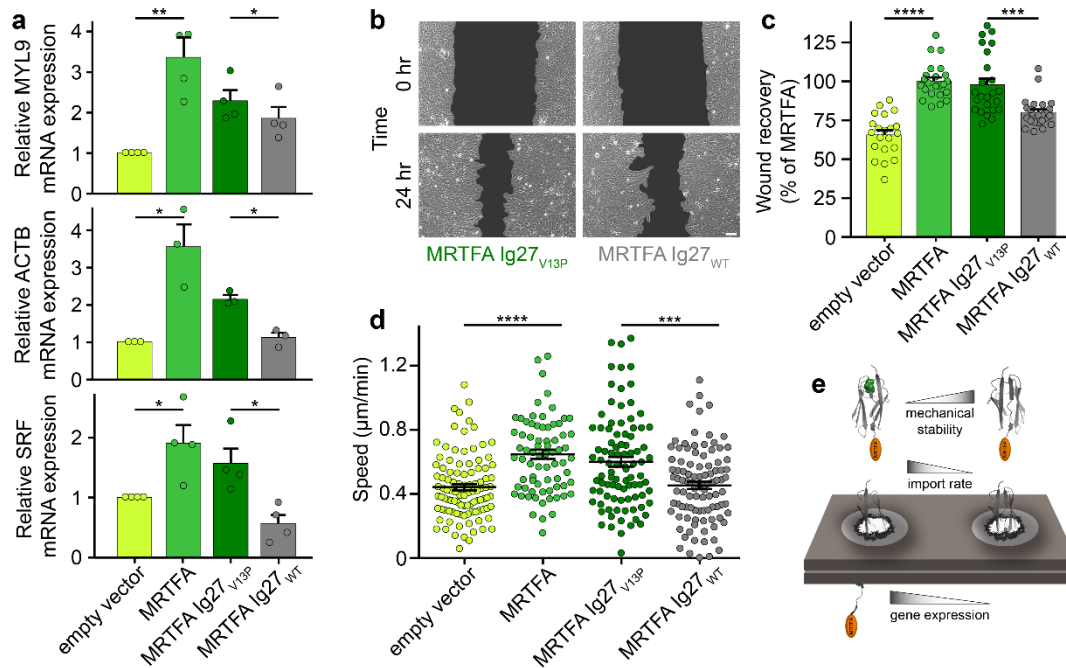
24

Figure 5. Mechanically-stable MRTFA constructs downregulate gene expression and cellular motility. (a) Real-time quantitative PCR in U2OS cells stably expressing a GFP empty vector, MRTFA-GFP, MRTFA-Ig27$_{WT}$-GFP or MRTFA-Ig27$_{V13P}$-GFP, 4 hours after serum stimulation. MYL9, ACTB and SRF gene expression is significantly higher when MRTFA is tagged with the mechanically-labile Ig27$_{V13P}$ domain compared to the mechanically-stable I27$_{WT}$. Data are from four (MYL9 and SRF) or three (ACTB) independent experiments, bars show mean ± s.e.m. Data were transformed using the log transformation y=log(y) to make data conform to normality and analysed using Paired *t*-test. **(b)** Representative bright-field images of wound healing of MRTFA-Ig27$_{V13P}$-GFP and MRTFA-Ig27$_{WT}$-GFP stable cell lines. 100 μm scale bar. **(c)** Wound-healing assays on U2OS stable cell lines show that wound recovery is significantly slower in cells expressing MRTFA-Ig27$_{WT}$-GFP compared to MRTFA-Ig27$_{V13P}$-GFP. Data are from three independent experiments (GFP empty vector, *n* = 21; MRTFA-GFP, *n* = 23; MRTFA-Ig27$_{V13P}$-GFP, *n* = 24; MRTFA-Ig27$_{WT}$-GFP, *n* = 24), bars show mean ± s.e.m. **(d)** Motility assays of MDA-MB-231 cells showing that the migration speed of cells transfected with MRTFA-Ig27$_{V13P}$-GFP is significantly higher than those transfected with MRTFA-Ig27$_{WT}$-GFP. Data are from three independent experiments (GFP empty vector, *n* = 101; MRTFA-GFP, *n* = 74; MRTFA-Ig27$_{V13P}$-GFP, *n* = 92; MRTFA-Ig27$_{WT}$-GFP, *n* = 98), bars show mean ± s.e.m. All statistical tests are two-tailed *t*-tests, * $P \leq 0.05$, ** $P \leq 0.01$, *** $P \leq 0.001$, and **** $P \leq 0.0001$. **(e)** Schematic representation of the proposed nuclear import mechanism by which the mechanical properties of the translocating protein regulate their nuclear shuttling dynamics.